Asymptotic normalization coefficients for $^{10}B \rightarrow {}^{9}Be + p$

A. M. Mukhamedzhanov, H. L. Clark, C. A. Gagliardi, Y.-W. Lui, L. Trache, R. E. Tribble, H. M. Xu, and X. G. Zhou
Cyclotron Institute, Texas A&M University, College Station, Texas 77843

V. Burjan, J. Cejpek, and V. Kroha
Institute for Nuclear Physics, Czech Academy of Sciences, Prague-Rez, Czech Republic

F. Carstoiu
Institute of Atomic Physics, Bucharest, Romania

(Received 13 March 1997)

The differential cross sections for the reactions $^{9}Be(^{10}B,^{10}B)^{9}Be$ and $^{9}Be(^{10}B,^{9}Be)^{10}B$ have been measured at an incident energy of 100 MeV. The elastic scattering data have been used to determine the optical model parameters for the $^{9}Be+{}^{10}B$ system at this energy. These parameters are then used in distorted-wave Born approximation (DWBA) calculations to predict the cross sections of the $^{9}Be(^{10}B,^{9}Be)^{10}B$ proton exchange reaction, populating the ground and low-lying states in ^{10}B. By normalizing the theoretical DWBA proton exchange cross sections to the experimental ones, the asymptotic normalization coefficients (ANC's), defining the normalization of the tail of the ^{10}B bound state wave functions in the two-particle channel $^{9}Be+p$, have been found. The ANC for the virtual decay $^{10}B(g.s.) \rightarrow {}^{9}Be+p$ will be used in an analysis of the $^{10}B(^{7}Be,^{8}B)^{9}Be$ reaction to extract the ANC's for $^{8}B \rightarrow {}^{7}Be+p$. These ANC's determine the normalization of the $^{7}Be(p,\gamma)^{8}B$ radiative capture cross section at very low energies, which is crucially important for nuclear astrophysics. [S0556-2813(97)02109-2]

PACS number(s): 25.70.Hi, 21.10.Jx, 24.10.Ht, 25.70.Bc

I. INTRODUCTION

Despite considerable experimental and theoretical progress in determining astrophysical nuclear reaction rates, there are still many problems to be solved, and new approaches are highly encouraged. One such approach follows from the peripheral character of many important astrophysical radiative capture reactions—such as $^{7}Be+p \rightarrow {}^{8}B+\gamma$, $\alpha+d \rightarrow {}^{6}Li+\gamma$, $\alpha+t \rightarrow {}^{7}Li+\gamma$, $\alpha+{}^{3}He \rightarrow {}^{7}Be+\gamma$, $^{8}B+p \rightarrow {}^{9}C+\gamma$, $^{12}C+\alpha \rightarrow {}^{16}O^{*}+\gamma$, and others. The overall normalization of the astrophysical S factor for each such reaction may be determined from one quantity, the asymptotic normalization coefficient (ANC) of the overlap function of the bound state wave functions of the initial and final particles [1,2]. The ANC's can be found, for example, from (i) analysis of classical nuclear reactions such as elastic scattering (by extrapolation of the experimental scattering phase shifts to the bound state pole in the energy plane [3,4]) or peripheral transfer reactions whose amplitudes contain the same overlap function as the amplitude of the corresponding astrophysical radiative capture process [5,6]; (ii) theoretical calculations [7].

The concept of the ANC turns out to be very useful in the determination of the overall normalization of astrophysical cross sections which are difficult to measure in direct experiments due to very low cross sections at energies of astrophysical interest. The most notorious among such reactions is $^{7}Be(p,\gamma)^{8}B$, occurring in the third p-p chain of hydrogen burning of main-sequence stars. Its reaction rate is of fundamental importance, both for calculating the high-energy solar neutrino flux, which is of special interest for the high-energy solar neutrino problem, and for defining the branching ratios between the different p-p chains. At astrophysical energies ($E_{c.m.} < 25$ keV), the cross section for this reaction is so small that its measurement has not been possible to date. In our work [1,2], we have pointed out that, due to the peripheral character of the $^{7}Be(p,\gamma)^{8}B$ reaction, the cross section for this reaction or, equivalently, the astrophysical factor $S_{17}(0)$ is determined solely by the ANC's for the virtual decay $^{8}B \rightarrow {}^{7}Be+p$. We also estimated $S_{17}(0)$ using the simple relation between the theoretical ANC's for the virtual decay $^{8}B \rightarrow {}^{7}Be+p$ [2] and $S_{17}(0)$.

The intriguing situation surrounding the S_{17} factor—especially after the first ^{8}B Coulomb breakup experiment [8], our calculations [1,2], and an R-matrix analysis [9] have all given a lower value for $S_{17}(0)$ than those used in predictions of the high-energy solar neutrino flux—calls for further experiments. The introduction of the ANC allows the use of transfer reactions to determine $S_{17}(0)$ by measuring its absolute value at zero energy directly with no need for extrapolation. Experiments to extract the ANC's for $^{8}B \rightarrow {}^{7}Be+p$ using different peripheral proton transfer reactions induced by ^{7}Be radioactive beams have been proposed by us [5,6]. To extract the ANC's for $^{8}B \rightarrow {}^{7}Be+p$, we are planning to measure the cross sections of the proton transfer reactions $^{10}B(^{7}Be,^{8}B)^{9}Be$ at incident ^{7}Be energies of ~ 90 MeV.

The idea of using proton transfer reactions induced by light heavy ions at energies above the Coulomb barrier to extract ANC's is based on their peripheral character. For such reactions, the cross section can be parametrized in terms of the product of the square of the ANC's corresponding to proton removal from the initial and final nuclei. Hence to find, for example, the ANC's for $^{8}B \rightarrow {}^{7}Be+p$ from the $^{10}B(^{7}Be,^{8}B)^{9}Be$ reaction, we have to know the ANC for the virtual decay $^{10}B \rightarrow {}^{9}Be+p$. Therefore, we have started the

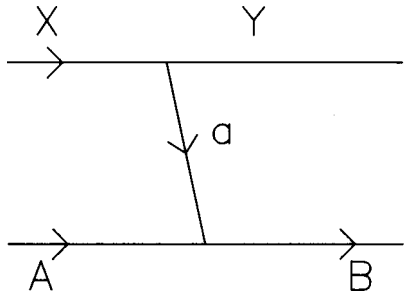

FIG. 1. The pole diagram describing particle a transfer.

cycle of experiments to determine the ANC's for $^8\mathrm{B}\rightarrow{}^7\mathrm{Be}+p$ with measurements of the elastic scattering $^{10}\mathrm{B}+{}^9\mathrm{Be}\rightarrow{}^{10}\mathrm{B}+{}^9\mathrm{Be}$ and of the proton transfer reaction $^9\mathrm{Be}(^{10}\mathrm{B},^9\mathrm{Be})^{10}\mathrm{B}$. The $^9\mathrm{Be}(^{10}\mathrm{B},^9\mathrm{Be})^{10}\mathrm{B}$ reaction has been chosen because the same ANC appears at both vertices of the elastic proton exchange amplitude (Fig. 1). Hence no other reaction is needed to obtain the ANC for $^{10}\mathrm{B}\rightarrow{}^9\mathrm{Be}+p$. The $^{10}\mathrm{B}+{}^9\mathrm{Be}$ elastic scattering data are needed to specify the optical potential parameters for the distorted-wave Born approximation (DWBA) analysis of the proton transfer reaction. The DWBA cross section for the proton transfer reaction is proportional to the ANC for $^{10}\mathrm{B}(\mathrm{g.s.})\rightarrow{}^9\mathrm{Be}+p$ to the fourth power. This ANC can be found by normalizing the DWBA differential cross section to the experimental one at small angles where the proton transfer mechanism is dominant. In addition to the primary purpose of using the ANC for $^{10}\mathrm{B}(\mathrm{g.s.})\rightarrow{}^9\mathrm{Be}+p$ in the measurement of the ANC's for $^8\mathrm{B}\rightarrow{}^7\mathrm{Be}+p$, the ANC's for the virtual decays of the ground and low-lying states of $^{10}\mathrm{B}$ may be used to calculate the direct part of the $^9\mathrm{Be}(p,\gamma)^{10}\mathrm{B}$ radiative capture reaction, which is quite controversial at present [10,11].

Nucleon exchange reactions between $1p$-shell heavy ions at energies below the Coulomb barrier have previously been used to extract ANC's [12–14]. At low energies the elastic scattering amplitude, peaked at forward angles, interferes strongly with the nucleon elastic exchange amplitude, which is large in the backward hemisphere. This interference causes oscillations in the angular dependence of the differential cross section at intermediate angles. The ANC's have been found by fitting the calculated cross sections to the experimental one in this intermediate angular region. In [15], the proton elastic exchange cross sections for the reaction $^9\mathrm{Be}(^{10}\mathrm{B},^9\mathrm{Be})^{10}\mathrm{B}$ were measured at center-of-mass energies of 9.5 and 14.5 MeV, which exceed the Coulomb barrier ($\sim$7 MeV). At energies slightly above the Coulomb barrier, the advantage of sub-Coulomb transfer is lost. The angular distributions, in contrast to the sub-Coulomb exchange reactions, have a sharp backward peak which is poorly reproduced by the DWBA proton exchange amplitude, while the interference between elastic scattering and elastic proton exchange at intermediate angles is not so pronounced as at sub-Coulomb energies. Meanwhile, these energies are not high enough to have the pole mechanism completely dominant at backward angles.

At energies well above the Coulomb barrier, the situation is different. The elastic scattering and direct elastic exchange amplitudes are strongly peaked in the forward and backward hemispheres, respectively, and both fall off sharply at intermediate angles. Interference between the two amplitudes is practically negligible, especially at backward angles. In Sec. III, we show that at 100 MeV, the $^{10}\mathrm{B}+{}^9\mathrm{Be}$ elastic cross section falls by four orders of magnitude in the angular interval $\theta_{\mathrm{c.m.}}=5^\circ-60^\circ$ and the elastic exchange cross section falls by almost three orders of magnitude in the angular region $\theta_{\mathrm{c.m.}}=180^\circ-120^\circ$. Hence, (1) in the intermediate region both amplitudes are very small, in contrast to the low-energy case, and (2) the influence of the elastic amplitude on the proton exchange amplitude at backward angles is negligible (the elastic exchange cross section in the angular interval $\theta_{\mathrm{c.m.}}=160^\circ-180^\circ$ exceeds the elastic cross section by eight orders of magnitude). Furthermore, due to the strong absorption, the pole mechanism is dominant. Thus, in Sec. V we find that the experimental angular distributions are very well reproduced by DWBA calculations.

Below we outline the theoretical approach that has been used to extract the ANC's. Then we discuss details of the experiment, an optical model analysis of the elastic scattering data, and our results for the ANC's.

II. THEORETICAL APPROACH: MODIFIED DWBA

Heavy-ion nucleon transfer reactions at energies above the Coulomb barrier have been utilized extensively for more than a decade to extract spectroscopic information. A vast majority of the efforts were intended to measure spectroscopic factors. The analysis has usually been done within the framework of the DWBA. It was understood that the extracted spectroscopic factors, also called empirical spectroscopic factors, depend strongly on model parameters—especially on the geometric parameters of the Woods-Saxon potentials used to calculate the bound state wave functions. However, there is another important fundamental nuclear parameter which can be extracted from heavy-ion data and which is much less model dependent than the spectroscopic factors, the asymptotic normalization coefficient. This originates from the peripheral character of nucleon transfer reactions induced by heavy ions.

Here we present the theoretical scheme for analysis of peripheral charged particle transfer reactions to extract ANC's within the framework of the DWBA. Consider the reaction

$$X+A\rightarrow Y+B, \tag{1}$$

where $X=Y+a$, $B=A+a$, and a is the transferred particle. The DWBA approach is based on the assumptions that (i) the simplest pole diagram, Fig. 1, describes the particle a transfer mechanism, at least near the main peak in the angular distribution; (ii) rescattering effects of the interacting particles in the initial and final states must be taken into account. The DWBA amplitude for the reaction (1) is given by

$$M(E_i,\cos\theta)=\sum_{M_a}\langle\chi_f^{(-)}I_{Aa}^B|\Delta V|I_{Ya}^X\chi_i^{(+)}\rangle. \tag{2}$$

Here, E_i is the relative kinetic energy of particles X and A, θ is the scattering angle in the center of mass, $\chi_i^{(+)}$ and $\chi_f^{(-)}$ are the distorted waves in the initial and final channels, and the transition operator is

$$\Delta V=V_{Ya}+V_{YA}-V_f \tag{3}$$

in the post form and

$$\Delta V = V_{Aa} + V_{YA} - V_i \tag{4}$$

in the prior form. $V_{\beta\gamma} = V^N_{\beta\gamma} + V^C_{\beta\gamma}$ is the interaction potential between particles β and γ, equal to the sum of the nuclear and Coulomb potentials, and V_i and V_f are the optical potentials in the initial and final channels. When deriving Eq. (2), it was assumed that $V_{\beta\gamma}$ depends only on the distance between the centers of mass of particles β and γ and does not depend on the coordinates of the constituent nucleons. For surface reactions, the part of the transition operator $V_{YA} - V_i$ ($V_{YA} - V_f$) can be approximated by the Coulomb part $V^C_{YA} - V^C_i$ ($V^C_{YA} - V^C_f$). The sum in Eq. (2) is taken over the spin projections M_a of the transferred particle a. The overlap function I of the bound state wave functions of particles α, β, and γ, where $\alpha = (\beta\gamma)$ is the bound state of particles β and γ, is given by

$$\begin{aligned} I^{\alpha}_{\beta\gamma}(\mathbf{r}_{\beta\gamma}) &= \langle \varphi_\beta(\zeta_\beta)\varphi_\gamma(\zeta_\gamma) | \varphi_\alpha(\zeta_\beta, \zeta_\gamma; \mathbf{r}_{\beta\gamma}) \rangle \\ &= \sum_{l_\alpha m_{l_\alpha} j_\alpha m_{j_\alpha}} \langle J_\beta M_\beta j_\alpha m_{j_\alpha} | J_\alpha M_\alpha \rangle \\ &\quad \times \langle J_\gamma M_\gamma l_\alpha m_{l_\alpha} | j_\alpha m_{j_\alpha} \rangle i^{l_\alpha} Y_{l_\alpha m_{l_\alpha}}(\hat{\mathbf{r}}_{\beta\gamma}) I^{\alpha}_{\beta\gamma l_\alpha j_\alpha}(r_{\beta\gamma}), \end{aligned} \tag{5}$$

where for each nucleus φ is the bound state wave function, ζ are a set of internal coordinates including spin-isospin variables, J and M are the spin and spin projection. Also $\mathbf{r}_{\beta\gamma}$ is the relative coordinate of the center of mass of nuclei β and γ, $\hat{\mathbf{r}} = \mathbf{r}/r$, j_α, m_{j_α} are the total angular momentum of particle γ and its projection in the nucleus $\alpha = (\beta\gamma)$, l_α, m_{l_α} are the orbital angular momentum of the relative motion of particles β and γ in the bound state $\alpha = (\beta\gamma)$ and its projection, $\langle j_1 m_1 j_2 m_2 | j_3 m_3 \rangle$ is a Clebsch-Gordan coefficient, $Y_{l_\alpha m_\alpha}(\hat{\mathbf{r}}_{\beta\gamma})$ is a spherical harmonic, and $I^{\alpha}_{\beta\gamma l_\alpha j_\alpha}(r_{\beta\gamma})$ is the radial overlap function. The antisymmetrization factor due to identical nucleons has been absorbed in the radial overlap function. The summation over l_α and j_α is carried out over the values allowed by angular momentum and parity conservation in the virtual process $\alpha \to \beta + \gamma$. Usually the radial overlap function is approximated by a model wave function of the bound state $\alpha = (\beta\gamma)$ as

$$I^{\alpha}_{\beta\gamma l_\alpha j_\alpha}(r_{\beta\gamma}) = S^{1/2}_{\beta\gamma l_\alpha j_\alpha} \varphi_{n_\alpha l_\alpha j_\alpha}(r_{\beta\gamma}). \tag{6}$$

Here $\varphi_{n_\alpha l_\alpha j_\alpha}(r_{\beta\gamma})$ is the bound state wave function of the relative motion of β and γ and $S_{\beta\gamma l_\alpha j_\alpha}$ is the spectroscopic factor of the configuration $(\beta\gamma)$ with quantum numbers l_α, j_α in nucleus α.

The cross section in the conventional DWBA is parametrized in terms of the product of the spectroscopic factors of the initial and final nuclei and can be written in the form [16]

$$\frac{d\sigma}{d\Omega} = \sum_{j_B j_X} S_{Aa l_B j_B} S_{Y a l_X j_X} \sigma^{\mathrm{DW}}_{l_B j_B l_X j_X}, \tag{7}$$

where $\sigma^{\mathrm{DW}}_{l_B j_B l_X j_X}$ is the reduced DWBA cross section. For simplicity, we assumed that only one value of l contributes to the reaction at each vertex. Since $\sigma^{\mathrm{DW}}_{l_B j_B l_X j_X}$ depend on the optical potential parameters and the geometric parameters of the Woods-Saxon potentials used to calculate the bound states, the extracted values of the phenomenological spectroscopic factors are also model dependent. The parameters of the optical potentials are usually fixed by analysis of elastic scattering data. It is well known that the results of such an analysis are ambiguous (see Sec. IV). But if the reaction is peripheral, the influence of the ambiguity of the optical model parameters on the value of the phenomenological spectroscopic factors is not very significant. The largest uncertainty in the absolute value of the spectroscopic factors arises from the strong dependence of the calculated DWBA cross section $\sigma^{\mathrm{DW}}_{l_B j_B l_X j_X}$ on the geometric parameters r_0, a of the bound state Woods-Saxon potentials used to determine the single-particle orbitals, which cannot be determined unambigously from experimental data.

The normalization of the DWBA cross section in terms of spectroscopic factors has another problem, especially manifested for surface reactions. The spectroscopic factor is defined mainly by the behavior of the overlap function in the nuclear interior, while the dominant contribution to peripheral reactions comes from the surface and outer regions of nuclei. Hence the parametrization of the DWBA cross section in terms of spectroscopic factors is not justified for peripheral reactions. There exists, however, another model-independent and important piece of information about the overlap functions which is, in fact, contained in the experimental data and which can be used in the DWBA calculations. This is the asymptotic normalization coefficient $C^{\alpha}_{\beta\gamma l_\alpha j_\alpha}$ defining the amplitude of the tail of the radial overlap function $I^{\alpha}_{\beta\gamma l_\alpha j_\alpha}(r_{\beta\gamma})$ [17,2]:

$$I^{\alpha}_{\beta\gamma l_\alpha j_\alpha}(r_{\beta\gamma}) \overset{r_{\beta\gamma} > R_N}{\longrightarrow} C^{\alpha}_{\beta\gamma l_\alpha j_\alpha} \frac{W_{-\eta_\alpha, l_\alpha + 1/2}(2\kappa_{\beta\gamma} r_{\beta\gamma})}{r_{\beta\gamma}}, \tag{8}$$

where R_N is the nuclear interaction radius between β and γ, $W_{-\eta_\alpha, l_\alpha + 1/2}(2\kappa_{\beta\gamma} r_{\beta\gamma})$ is the Whittaker function describing the asymptotic behavior of the bound state wave function of two charged particles, $\kappa_{\beta\gamma} = \sqrt{2\mu_{\beta\gamma}\varepsilon_{\beta\gamma}}$ is the wave number of the bound state $\alpha = (\beta\gamma)$, $\mu_{\beta\gamma}$ is the reduced mass of particles β and γ, and $\eta_\alpha = Z_\beta Z_\gamma \mu_{\beta\gamma}/\kappa_{\beta\gamma}$ is the Coulomb parameter of the bound state $(\beta\gamma)$. The ANC $C^{\alpha}_{\beta\gamma l_\alpha j_\alpha}$ is related to the nuclear vertex constant (NVC) $G^{\alpha}_{\beta\gamma l_\alpha j_\alpha}$ by [17,18]

$$G^{\alpha}_{\beta\gamma l_\alpha j_\alpha} = -e^{i\pi[(l_\alpha + \eta_\alpha)/2]} \frac{\sqrt{\pi}}{\mu_\alpha} C^{\alpha}_{\beta\gamma l_\alpha j_\alpha}. \tag{9}$$

Note that we use the system of units with $\hbar = c = 1$. Taking into account the asymptotic behavior of the bound state wave function

$$\varphi_{n_\alpha l_\alpha j_\alpha}(r_{\beta\gamma}) \overset{r_{\beta\gamma} > R_N}{\longrightarrow} b_{\beta\gamma l_\alpha j_\alpha} \frac{W_{-\eta_\alpha, l_\alpha + 1/2}(2\kappa_{\beta\gamma} r_{\beta\gamma})}{r_{\beta\gamma}}, \tag{10}$$

where $b_{\beta\gamma l_\alpha j_\alpha}$ is the single-particle ANC defining the amplitude of the tail of the bound state wave function at large $r_{\beta\gamma}$, we easily derive from Eqs. (6), (8), and (10)

$$(C^{\alpha}_{\beta\gamma l_\alpha j_\alpha})^2 = S_{\beta\gamma l_\alpha j_\alpha} b^2_{\beta\gamma l_\alpha j_\alpha}. \tag{11}$$

Condition (11) introduces into the DWBA analysis additional physical information which is extremely important for two reasons. First, as we will see, Eq. (11) guarantees the correct absolute normalization of the peripheral DWBA amplitudes which give the dominant contribution to the cross section at small angles. Second, condition (11) allows one to significantly decrease the dependence of the calculated DWBA cross section on the geometric parameters r_0, a of the bound state Woods-Saxon potentials. For a peripheral reaction with fixed optical potential parameters in the initial and final channels, the ANC's may be taken as the only fitting parameters. For example, suppose the reaction is purely peripheral and only single values of j_X and j_B are allowed. In the traditional approach, the product of the spectroscopic factors is extracted by normalizing the DWBA cross section, Eq. (7), to the experimental one. Since $\sigma^{\rm DW}_{l_B j_B l_X j_X}$ is very sensitive to the adopted values of the geometric parameters of the Woods-Saxon potentials for the two bound states $X = Y + a$ and $B = A + a$, the extracted value of $S_{Aal_B j_B} S_{Yal_X j_X}$ is strongly dependent on the assumed geometry of the bound state potentials. By contrast, we can modify the conventional DWBA analysis to take into account the additional condition (11) fixing the correct normalization of the peripheral part of the cross section. Using (11) we can rewrite (7) as

$$\frac{d\sigma}{d\Omega} = \sum_{j_B j_X} \frac{(C^B_{Aal_B j_B})^2}{b^2_{Aal_B j_B}} \frac{(C^X_{Yal_X j_X})^2}{b^2_{Yal_X j_X}} \sigma^{\rm DW}_{l_B j_B l_X j_X}. \tag{12}$$

For peripheral reactions, only $r_{Ya} > R_X$ and $r_{Aa} > R_B$ contribute to the DWBA radial integrals, i.e., $\sigma^{\rm DW}_{l_B j_B l_X j_X}$ should be practically insensitive to the variation of the cutoff radii at $R_{\rm cut} < R_X$ in the initial channel and at $R_{\rm cut} < R_B$ in the final channel. Hence, each of the bound state wave functions entering the expression for $\sigma^{\rm DW}_{l_B j_B l_X j_X}$ can be approximated by its asymptotic form. The dependence on the geometry of the bound state potentials appears only through the product of the single-particle ANC's, $b_{Aal_B j_B} b_{Yal_X j_X}$, allowing us to write

$$\frac{d\sigma}{d\Omega} = \sum_{j_B j_X} (C^B_{Aal_B j_B})^2 (C^X_{Yal_X j_X})^2 R_{l_B j_B l_X j_X}, \tag{13}$$

where

$$R_{l_B j_B l_X j_X} = \frac{\sigma^{\rm DW}_{l_B j_B l_X j_X}}{b^2_{Aal_B j_B} b^2_{Yal_X j_X}} \tag{14}$$

is nearly independent of $b_{Aal_B j_B}$ and $b_{Yal_X j_X}$. Thus the introduction of condition (11) into the standard DWBA analysis guarantees the correct absolute normalization of the peripheral reaction cross section; it is actually parametrized in terms of the product of the square of the ANC's of the initial and final nuclei $(C^B_{Aal_B j_B})^2 (C^X_{Yal_X j_X})^2$, rather than spectroscopic factors. Furthermore, in this form, it is insensitive to the assumed geometries of the bound state potentials.

The independence of the DWBA cross section on the values of the single-particle ANC's $b_{Aal_B j_B}$ and $b_{Yal_X j_X}$ for purely peripheral reactions opens another possibility to check the peripheral character of the reaction under consideration. For a peripheral reaction, the cross section (13) will depend, at most, weakly on the geometry of the bound state Woods-Saxon potentials.

III. THE EXPERIMENT

The elastic scattering and transfer reaction measurements were carried out at the Texas A&M University K500 superconducting cyclotron facility. The multipole-dipole-multipole (MDM) magnetic spectrometer, formerly at Oxford [19], was used to analyze the reaction products. The $^{10}B^{+2}$ beam at $E = 100$ MeV was prepared using the newly installed beam analysis system [20], which allows for the control of the energy and angular spread of the beam. Self-supported ^{9}Be targets, between $200-300$ μg/cm^2 thick, obtained by evaporation, were placed perpendicular to the beam in the sliding-seal target chamber of the MDM. The magnetic field of the spectrometer was set to transport either $^{10}B^{+5}$ ions, to measure elastic scattering, or $^9Be^{+4}$, to measure the proton transfer reaction, to its focal plane, where the particles were observed in the modified Oxford detector [21]. There, the position of the particles along the dispersive x direction was measured with resistive wires at four different depths within the detector, separated by about 16 cm each. For particle identification we used the specific energy loss measured in the ionization chamber and the residual energy measured in a NE102A plastic scintillator located in air, just behind the exit window of the detector. The entrance and exit windows of the detector were made of 1.8 and 7.2 mg/cm^2 thick Kapton foils, respectively. The ionization chamber was filled with pure isobutane at a pressure of 30 Torr. The entire horizontal acceptance of the spectometer $\Delta\theta = \pm 2^\circ$ and a restricted vertical opening $\Delta\phi = \pm 0.5^\circ$ were used in this measurement. Raytracing was used to reconstruct the scattering angle in the analysis of the data. For this purpose, in addition to RAYTRACE calculations [22], angle calibration data were obtained at several angles by using an angle mask consisting of five openings of $\Delta\theta = \pm 0.05^\circ$, centered at -1.6°, -0.8°, 0°, $+0.8^\circ$, and $+1.6^\circ$ relative to the central angle of the spectrometer. By moving the spectrometer from $\theta_{\rm lab} = -3^\circ$ (past 0°) to 28° we covered the angular range $\theta_{\rm c.m.} = 0^\circ - 56^\circ$ for the proton exchange reaction. Elastic scattering data were obtained for the angular region $\theta_{\rm c.m.} = 8^\circ - 64^\circ$. Typically we rotated the spectrometer by 2° at a time, allowing for an angle overlap that provided a self-consistency check of the data at all angles. Normalization of the data was done using current integration in a Faraday cup.

When increasing the angle of the spectrometer, the focal plane migrates from the back toward the front of the detector. Focal plane reconstruction was done at each angle using the position measured with the wire nearest to the focal plane and using the detector angle calculated from the positions

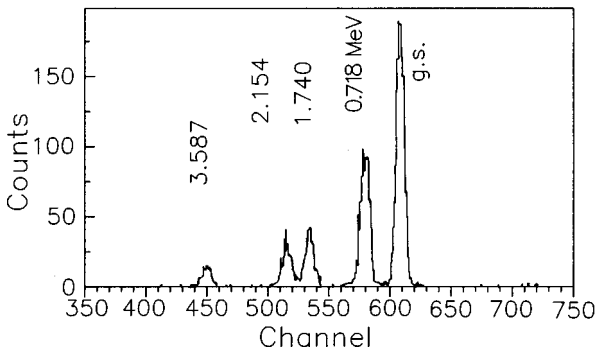

FIG. 2. Spectrum from the proton transfer reaction ^{9}Be(^{10}B,^{9}Be)^{10}B at $E=100$ MeV, taken at $\theta_{lab}=4°$. The excitation energies in ^{10}B, in MeV, are marked on the peaks.

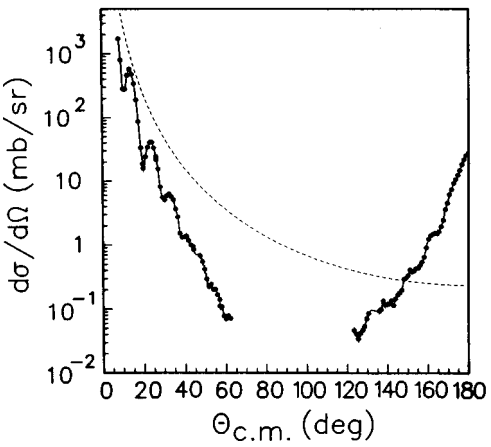

FIG. 3. The angular distribution for elastic scattering of 100 MeV ^{10}B on ^{9}Be is shown over the whole angular range $\theta_{c.m.}=0°-180°$. The data at forward angles were obtained by measuring the elastically scattered ^{10}B nuclei. Those at backward angles were obtained by measuring the ''recoiling'' ^{9}Be nuclei at the complementary forward angles. The dashed line is the Rutherford scattering differential cross section. The solid line is merely to guide the eye.

measured at all four wires. As an additional constraint on the data, a gate was set on the difference between the detector angles found from two different pairs of wires. Finally, the scattering angle and the position at the focal plane were determined from the raw data by raytracing each event. The angular range of 4° covered by the acceptance slit was divided into eight bins, resulting in eight points in the angular distribution being measured simultaneously.

The measurements with the angle mask showed that the scattering angle resolution in the laboratory frame was 0.25° full width at half maximum (FWHM). This includes a contribution from the angular spread of the beam of about 0.1° FWHM. The energy resolution obtained in both reactions was ~150 keV FWHM at forward angles. It degraded as we advanced to larger angles, due to the large kinematic factors $k=(1/p)dp/d\theta$ coupled with the finite angular spread in the beam. In the proton exchange reaction, peaks corresponding to the elastic proton transfer channel and to the inelastic transfer to the first four excited states of ^{10}B can be identified, as seen in Fig. 2. Only the transitions to the ground state and the first three excited states were observed with adequate statistics over the whole angle range to obtain good angular distributions.

During the experiment, particular emphasis was placed on obtaining accurate absolute values for the cross sections by a careful evaluation of the normalization of the elastic scattering. In addition to statistical errors which were very small at forward angles and increased to about 5% at larger angles, we found from our consistency checks that a 3% uncertainty must be included to account for procedural uncertainties, such as the central angle reading, the angle binning, and charge collection accuracy. Very small amounts of heavy impurities in the Be target, most likely Ta from the preparation of the target, along with Ca, O, and C, dominate the elastic scattering at very small angles (below $\theta_{lab}=4°$) and prevented us from using a straightforward normalization of the elastic scattering on ^{9}Be to Rutherford scattering. Two other independent approaches were used instead to obtain the absolute normalization of the cross sections. In the first, we carried out measurements to determine target thicknesses and charge collection efficiencies in the Faraday cup by using a gold target of about 200 μg/cm^2 thickness at a central angle of 6°, where elastic scattering on gold is purely Rutherford at this energy. Target thicknesses were determined from the measured energy loss of the ^{10}B beam in the ^{9}Be target and of both ^{10}B and ^{9}Be in the Au target, using the MDM spectrometer. Specific energy losses in Au and Be targets were calculated using the code TRIM [23]. A 9% accuracy was assigned to the absolute values of the cross sections determined with this normalization, due mostly to the precision in determining the thickness of the Au target. The second approach consisted of a comparison of the elastic scattering data at the most forward angles with calculations of optical model fitting programs. It is based on the observation that heavy-ion elastic scattering angular distributions at forward angles are less sensitive to the precise shape and magnitude of the nuclear part of the potential. Using only the data at very forward angles (the first nine points) in a χ^2 minimization procedure, we determined an overall normalization constant with a relative uncertainty of 9%, based upon the changes in the χ^2 values when the normalization varies. The normalization found coincides with the first one within 2%. Combining the results of these two independent determinations, we conclude that we have an overall normalization accuracy of 7% for the absolute values of the cross sections for both the ^{9}Be(^{10}B,^{10}B)^{9}Be elastic scattering data and the ^{9}Be(^{10}B,^{9}Be)^{10}B proton transfer data.

Measuring ^{9}Be nuclei at forward angles is kinematically equivalent with measuring the elastic scattering of ^{10}B in the backward hemisphere, provided that no energy is lost in the nuclear process. Therefore we plot in Fig. 3 the cross section for elastic scattering of ^{10}B on ^{9}Be, using the data from the detection of ^{10}B in the forward hemisphere and the data from the detection of the ''recoiling'' ^{9}Be nuclei at complementary forward angles in the backward hemisphere. The rise in the cross section at backward angles shows clearly that we have a contributing mechanism that is different from potential scattering and can only be explained by the transfer of one proton between the target and projectile. It is clear that the elastic scattering and elastic transfer cross sections are dominant in completely different angular ranges with negligible interference.

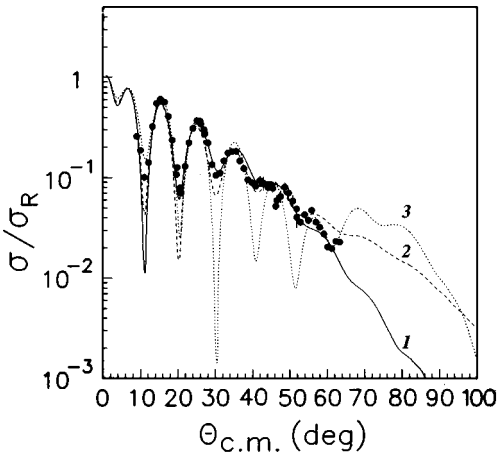

FIG. 4. The fits of the elastic scattering cross section of 100 MeV ^{10}B on ^{9}Be in the forward hemisphere. The solid, dashed, and dotted curves are the calculations for optical potentials 1, 2, and 3 (Table I), respectively.

The ^{9}Be(^{10}B,^{10}B)^{9}Be elastic scattering angular distribution (the forward angles in Fig. 3) is shown in Fig. 4. The angular distribution measured for the elastic exchange reaction (the backward angles in Fig. 3) is plotted in Fig. 5. The angular distributions for the inelastic proton transfer to the first excited state of ^{10}B—$J^{\pi}=1^{+}$, $T=0$, $E^{*}=0.718$ MeV—is shown in Fig. 6, that for the second excited state—$J^{\pi}=0^{+}$, $T=1$, $E^{*}=1.740$ MeV—is shown in Fig. 7, and that for the third excited state—$J^{\pi}=1^{+}$, $T=0$, $E^{*}=2.154$ MeV—is shown in Fig. 8. The curves represent DWBA fits and will be discussed in Secs. IV and V.

IV. EXTRACTION OF OPTICAL MODEL PARAMETERS

The elastic scattering data have been fit using the code OPTIMINIX [24] in a standard optical model analysis using Woods-Saxon volume form factors with the usual notation:

$$U(r)=-[Vf_V(r)+iWf_W(r)], \tag{15}$$

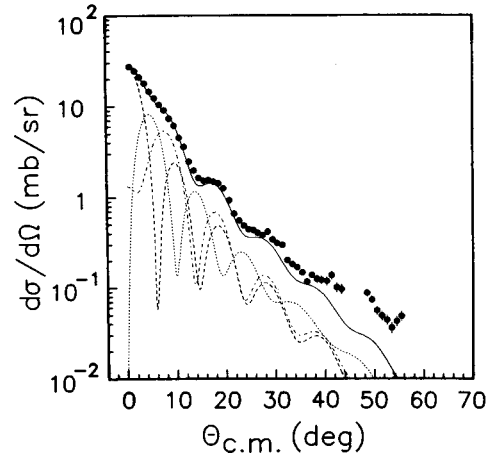

FIG. 5. The experimental and calculated angular distributions for the reaction ^{9}Be(^{10}B,^{9}Be)^{10}B(g.s.). The points are experimental data; the solid line is the DWBA fit made with optical potential 1. The individual contributions of $l_{\rm tr}=0,1,2$ are presented by dashed, dotted, and dashed-dotted lines, respectively. Optical potential 2 gives the same fitted result.

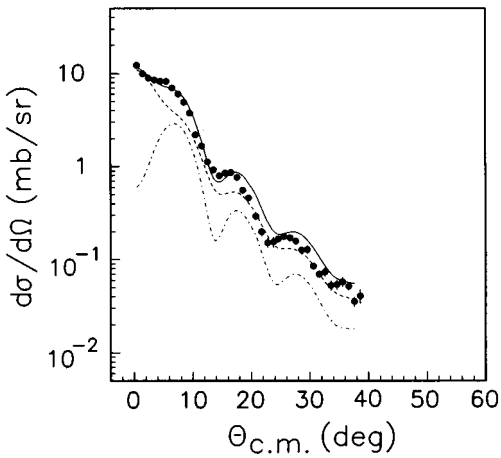

FIG. 6. The experimental and calculated angular distributions for the reaction ^{9}Be(^{10}B,^{9}Be)^{10}B(0.718 MeV). The points are experimental data; the solid line is the DWBA fit. The dashed line is the $j_X=3/2\rightarrow j_B=3/2$ component of the DWBA cross section; the dash-dotted line is the $j_X=3/2\rightarrow j_B=1/2$ component. The calculations have been done with optical potential 1.

where

$$f_x(r)=\left[1+\exp\left(\frac{r-r_x(A_1^{1/3}+A_2^{1/3})}{a_x}\right)\right]^{-1} \tag{16}$$

and $x=V,W$ stands for the real and imaginary (volume) parts of the potentials, respectively. Only the central components have been included in the optical potential, since vector and higher rank tensor spin-orbit couplings were found to have little or no influence on the cross sections.

The fits of the elastic scattering data in the forward hemisphere using three different optical parameter sets are shown in Fig. 4. The three sets of optical potential parameters are given in Table I. J_V and J_W in Table I are the volume integrals for the real and imaginary parts of the potentials and σ_R is the total reaction cross section. The parameters were obtained by griding the initial depth of the real potential in small steps in the range from 50 to 250 MeV, in order to identify the local minima, and then searching for minima on

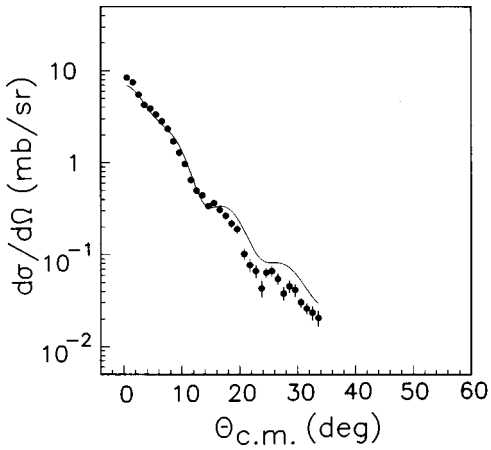

FIG. 7. The experimental and calculated angular distributions for the reaction ^{9}Be(^{10}B,^{9}Be)^{10}B(1.740 MeV). The points are experimental data; the solid line is the DWBA calculation made with optical potential 1.

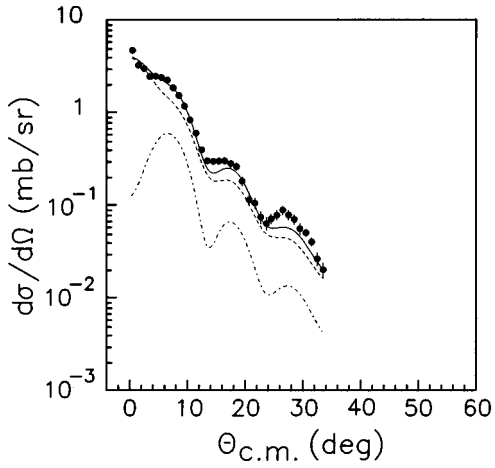

FIG. 8. The experimental and calculated angular distributions for the reaction ^{9}Be(^{10}B,^{9}Be)^{10}B(2.154 MeV). The points are experimental data; the solid line is the DWBA fit. The dashed line is the $j_X=3/2\rightarrow j_B=3/2$ component of the DWBA cross section; the dashed-dotted line is the $j_X=3/2\rightarrow j_B=1/2$ component. The calculations have been done with optical potential 1.

all parameters with no constraints. Three families of potentials were found using this technique. A characteristic jump of 70 MeV fm^3 in the volume integral of the real part of the optical potential serves to identify these potentials as discrete members of a sequence of potentials which give nearly comparable descriptions of the data. The members of each family of potentials are connected by the well-known continuous Igo ambiguity $V\exp(R_V/a_V)=C$ [25].

The absorption is seen to be independent of the strength and shape of the real part of the optical potential and, as a consequence, the reaction cross section is constant along the sequence. Potential number 3 has a real volume integral of $\simeq$500 MeV fm^3, which suggests that intermediate members of the sequence were missed in the analysis, most probably due to the unconstrained searching procedure. Fits using the codes PTOLEMY [26] and ECIS [27] gave similar results.

From the general trend of the data, it appears that potential 1, which has the smallest χ^2, provides the most realistic description of the scattering, and potential 3 can be rejected. In the angular range covered, the prediction of potential 2 for the elastic scattering differs from that of potential 1 primarily in the depths of its minima. We also note that it was found earlier that the typical optical potentials needed to describe transfer data in reactions involving p-shell nuclei at energies above 80 MeV have depths of the real potential well in the range of $V\simeq 50-100$ MeV [16]. This would exclude potential 3 as far too deep. While our elastic scattering data tend to prefer potential 1, we have chosen to use both potentials 1 and 2 in the extraction of ANC's in the next section in order to evaluate our sensitivity to the optical model parameters.

In addition to the phenomenological optical potential of the Woods-Saxon form, we have found a microscopic optical potential from the double folding procedure using the $M3Y$ effective NN interaction [28]. We fit this potential with the Woods-Saxon shape at distances $r>4.5$ fm which is the region that provides the overwhelming contribution to the proton transfer reaction ^{9}Be(^{10}B,^{9}Be)^{10}B at forward angles (see next section). The Woods-Saxon form that fits the microscopic folding potential has a depth of the real part of 49.8 MeV and gives a DWBA cross section which nearly coincides with the cross section calculated for optical potential 1.

V. ANALYSIS OF THE PROTON EXCHANGE DATA

The process used to extract angular distributions for the proton exchange reactions was described above. The analysis of the proton exchange data has been done using the PTOLEMY [26] and LOLA [29] DWBA codes. Both gave the same results. The calculations have been done with the full transition operator given by Eq. (3). (Post and prior forms are identical.) Since in the reaction ^{9}Be(^{10}B,^{9}Be)^{10}B the initial and final nuclei are the same, the same optical potential describes the scattering of particles in the entrance and exit channels. We performed the calculations with two different sets of optical potentials, as noted above. The results from the calculations are plotted with the data. The angular distributions measured for the elastic proton exchange reaction and for the inelastic proton transfer to the first three excited states of ^{10}B are plotted in Figs. 5 to 8, respectively.

The test of the peripheral character of the ^{9}Be(^{10}B,^{9}Be)^{10}B(g.s.) reaction has been made in two ways: (i) by changing the cutoff radius (lower limit in the radial integration over the distance between the colliding particles); (ii) by changing the geometric parameters r_0 and a of the bound state Woods-Saxon potentials, and hence the single-particle ANC's b, and calculating the dependence of the R function on b.

The basic calculations have been done with the Woods-Saxon potential for the bound states with geometric parameters $r_0=1.2$ fm, $a=0.6$ fm, and the Thomas spin-orbit term. However, due to the peripheral character of the reactions under consideration, the results are only weakly dependent on the geometry of the bound state Woods-Saxon potentials.

TABLE I. The parameters of the Woods-Saxon optical model potentials extracted from the analysis of the elastic scattering data for ^{10}B (100 MeV)+^{9}Be. We use standard notations: V and W are the depths of the real and imaginary (volume) potentials, r_V,a_V are the radius and diffuseness parameters of the real potential, and r_W,a_W are the radius and diffuseness parameters of the imaginary potential. The Coulomb radius parameter is $r_C=1.0$ fm for all potentials.

Pot.	V [MeV]	W [MeV]	r_V [fm]	r_W [fm]	a_V [fm]	a_W [fm]	χ^2	σ_R [mb]	J_V [MeVfm3]	J_W [MeV fm^3]
1	64.2	30.1	0.78	0.99	0.99	0.75	19.8	1318	206	136
2	131.2	29.7	0.67	0.95	0.90	0.86	45.4	1411	276	131
3	203.2	24.7	0.81	1.04	0.60	0.83	61.8	1428	499	133

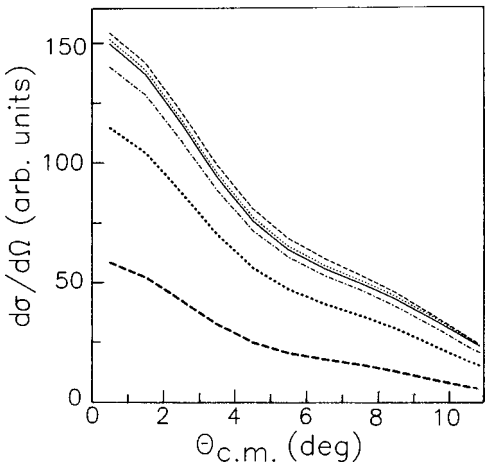

FIG. 9. The dependence of the DWBA differential cross section on the cutoff radius. The lines are the DWBA cross sections for the reaction ^{9}Be(^{10}B,^{9}Be)^{10}B for different cutoff radii: the solid line is for $R_{\rm cut}=0$ fm, the light dotted line for $R_{\rm cut}=4.0$ fm, the light dashed line for $R_{\rm cut}=5.0$ fm, the light dashed-dotted line for $R_{\rm cut}=5.5$ fm, the dark dotted line for $R_{\rm cut}=6.0$ fm, the dark dashed line for $R_{\rm cut}=7.0$ fm. The calculations have been done with the geometric parameters of the bound state Woods-Saxon potential $r_0=1.20$ fm, $a=0.60$ fm, and optical potential 1. Optical potential 2 gives similar results.

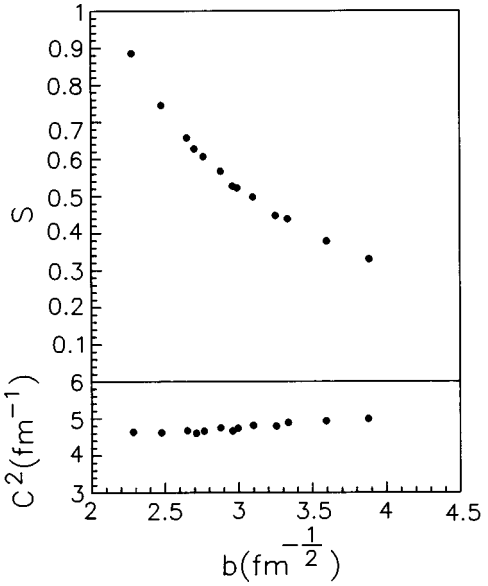

FIG. 11. The upper panel shows the dependence of the extracted spectroscopic factor S for the configuration ^{9}Be($3/2^-$) $+p(j_p=3/2^-)$ in ^{10}B(g.s.) on the single-particle ANC b. The lower panel shows the extracted ANC C^2 of the associated overlap function for the same values of b. Both calculations have been done using optical potential 1.

For the ground state transition, the proton binding energy in the initial and final ^{10}B nuclei is 6.587 MeV. The angular momenta associated with the two channels are [30] $J_X^\pi=J_B^\pi=3^+$, $J_Y^\pi=J_A^\pi=3/2^-$, $l_X=l_B=1$, $j_X=j_B=3/2$. Thus the allowed transfer orbital angular momenta are $l_{\rm tr}=0,1,2$. The $l_{\rm tr}=0$ component is overwhelmingly dominant and provides the peak in the angular distribution at 0° in full agreement with Brink conditions [31]. The experimental and calculated angular distributions for the reaction ^{9}Be(^{10}B,^{9}Be)^{10}B(g.s.) are presented in Fig. 5. The DWBA calculations have been made for the first two sets of optical potentials (Table I) found from the analysis of the elastic scattering data. For both potentials, the agreement of the theoretical angular distribution with the experimental one is excellent at forward angles $\theta_{\rm c.m.}<20°$. We note that the most important region to extract the ANC reliably is at small angles (or $\cos\theta\sim1$) where the pole mechanism, Fig. 1, dominates. We also note that the calculated shape of the angular distribution does not depend on the geometry of the bound state Woods-Saxon potentials.

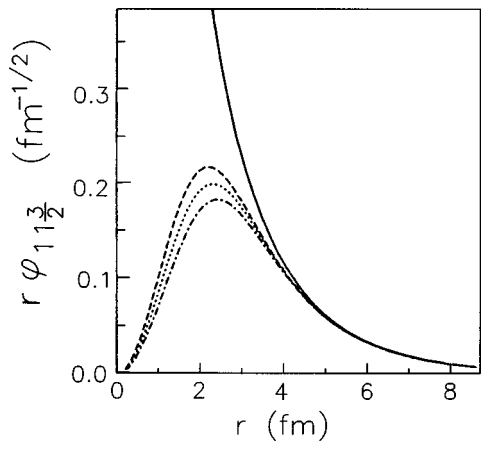

FIG. 10. The radial behavior of the single particle radial bound state proton wave functions $r\varphi_{n_X l_X j_X}(r)$, $n_X=1, l_X=1, j_X=3/2$, in ^{10}B calculated in the Woods-Saxon potentials with $a=0.60$ fm and $r_0=1.00$ fm, dashed line; $r_0=1.25$ fm, dotted line; $r_0=1.50$ fm, dashed-dotted line. The Coulomb radius $r_C=1.20$ fm. The solid line is the tail $bW_{-\eta_X,3/2}(2\kappa_{Ya}r)$ of the bound state wave function $r\varphi_{n_X l_X j_X}(r)$ for $r_0=1.00$ fm, $a=0.60$ fm, with $b=2.78$ fm$^{-1/2}$. The other two bound state wave functions are also normalized to that tail.

As noted above, we made calculations at different values of cutoff radius $R_{\rm cut}$ to check the peripheral character of the reaction. The dependence of the DWBA differential cross section on the cutoff radius is shown in Fig. 9. Calculations have been done for both adopted optical potentials 1 and 2 from Table I. Since the dependence of the cross section on $R_{\rm cut}$ is the same for both potentials, only the results for optical potential 1 are presented in the figure. We see that at $R_{\rm cut}\leqslant5$ fm the cross section is insensitive to the variation of cutoff radius, so the contribution from this region is practically negligible.

In Fig. 10 we present the radial behavior of the shell model bound state proton wave functions in ^{10}B calculated using the Woods-Saxon potential with three different radius parameters. We see that all of them reach their asymptotic form, given by the Whittaker function, for $r>4.5$ fm. Hence, when calculating the DWBA matrix element, the bound state wave function can be replaced by its asymptotic term. To verify this quantitatively, we also determined the dependence of the R function, Eq. (14), on the geometric parameters r_0 and a of the Woods-Saxon potentials used to calculate the single-particle bound state wave functions. Actually, for transfer reactions the R function is a functional depending on the single-particle ANC's, rather than on the individual values of r_0 and a. Increasing (decreasing) r_0 and/or a increases

TABLE II. Dependence of the DWBA cross section and R function on b for the reaction ^{9}Be(^{10}B,^{9}Be)^{10}B(g.s.). The calculations have been done with optical potential 1 at a scattering angle $\theta=0°$; r_0 and a are the geometric parameters of the bound state Woods-Saxon potentials. The Coulomb radius parameter is 1.2 fm.

r_0 [fm]	a [fm]	b [fm$^{-1/2}$]	C^2 [fm^{-1}]	$d\sigma^{DW}/d\Omega$ [mb/sr]	R
1.1	0.5	2.50	4.52	52.34	1.35
1.1	0.7	3.12	4.87	117.38	1.25
1.2	0.6	3.01	4.78	107.01	1.30
1.3	0.5	2.98	4.73	104.01	1.33
1.3	0.7	3.61	5.00	201.43	1.18

(decreases) b, while simultaneous changes of r_0 and a in opposite directions tend to compensate each other. As we have noted, for purely peripheral reactions the R function should be constant as a function of $b^2_{Aal_Bj_B}b^2_{Yal_Xj_X}$, and for the ground state transition $b=b_{Aal_Bj_B}=b_{Yal_Xj_X}$. By changing r_0 and a, we changed the values of the single-particle ANC b. For each value of b, we then determined the empirical spectroscopic factor S and the ANC C^2 of the overlap function for $^{10}\mathrm{B}\rightarrow\ ^9\mathrm{Be}+p$. The results are shown in Fig. 11. Due to the peripheral character of the reaction, C^2 changes by only $\approx 10\%$ while S changes by a factor of 3. The range of r_0,a represented by Fig. 11 is, in fact, much larger than typically considered. In Table II, we show the dependence of b, C^2, the reduced DWBA cross section $\sigma^{DW}_{l_Bj_Bl_Xj_X}$, and the R function at $\theta=0°$ on the parameters (r_0,a) in the standard region $1.1\leqslant r_0\leqslant 1.3$ fm and $0.5\leqslant a\leqslant 0.7$ fm. The uncertainty in R corresponding to the relative difference between the central value of R (for $r_0=1.2$ fm, $a=0.6$ fm) and the lowest and highest values for geometrical parameters varying in the standard region is $\pm 9\%$. The extracted value of C^4 is inversely proportional to R, so we assign an uncertainty of $\pm 4.5\%$ to our extracted value of C^2 to account for the variation of R with (r_0,a).

By normalizing the calculated DWBA cross section to the experimental one at forward angles, we find the values of the ANC for the virtual decay $^{10}\mathrm{B(g.s.)}\rightarrow{}^9\mathrm{Be}+p$. The results for the two different optical potentials are given in Table III. Since potential 1 gave a somewhat better description of the elastic scattering data, we chose to weight its value for C^2 twice that of potential 2 in specifying our best value, and we assign an uncertainty of $\pm 5\%$ to our adopted value of C^2 to account for the uncertainty in the choice of optical model parameters. The insensitivity of C^2 to the choice of optical model parameters is illustrated by the fact that, if we utilize optical potential 3, which clearly provides the poorest description of the elastic scattering data among the three potentials found and has a much deeper real part than typical of this region, the value of C^2 that we obtain is only $\sim 15\%$ larger than our adopted one.

To estimate the possible influence of multistep processes we evaluated the differential cross section for the reaction ^{9}Be(^{10}B,^{9}Be)^{10}B as a two-step process going through excited states of ^{9}Be at $5/2^-$,2.43 MeV, and $7/2^-$,6.76 MeV, that belong to the rotational band built on the $3/2^-$ ground state with $K^\pi=3/2^-$. The deformation parameters were found from the experimental $B(E2)$ values for $3/2^-\rightarrow 5/2^-$ and $3/2^-\rightarrow 7/2^-$ transitions [30]. If we assume that the reaction mechanism is described as the inelastic excitation of ^{9}Be with the subsequent proton pick-up leading to the ground state of ^{10}B, the two-step cross sections evaluated within the framework of the on-shell approximation give a correction to the one-step cross section which is about 3% for each transition. We also made calculations of the ^{9}Be(^{10}B,^{9}Be)^{10}B differential cross section using the coupled channels code CHUCK [32], including the coupling among the three states $3/2^-$,$5/2^-$,$7/2^-$ in ^{9}Be and the two states 3^+,4^+ of ^{10}B with parameters taken from [33]. We find that these calculations can be reproduced within the framework of the

TABLE III. The measured ANC's C^2 and NVC's $|G|^2$ for $^{10}\mathrm{B}\rightarrow{}^9\mathrm{Be}+p$ from ^{9}Be(^{10}B,^{9}Be)^{10}B reactions. C^2_1 and C^2_2 are the extracted ANC's using optical potentials 1 and 2, respectively, and bound state Woods-Saxon potentials with $r_0=1.20$ fm, $a=0.60$ fm. The uncertainties specified include only the contribution from the statistics in the angular distribution fits. C^2 and $|G|^2$ are our adopted values of the ANC's and NVC's. Their uncertainties include the contributions due to the normalization uncertainty and the theoretical systematic effects described in the text, in addition to the statistical uncertainties from the angular distribution fits.

E^* (MeV)	j_p	C^2_1 (fm^{-1})	C^2_2 (fm^{-1})	C^2 (fm^{-1})	$\lvert G\rvert^2$ (fm)
0.0	3/2	4.91(19)	5.35(21)	5.06(46)	0.87(8)
0.718	1/2	1.23(15)	1.34(16)	1.27(21)	0.22(4)
	3/2	3.33(17)	3.63(19)	3.43(42)	0.59(7)
1.740	3/2	4.22(33)	4.60(36)	4.35(59)	0.74(9)
2.154	1/2	0.28(5)	0.30(5)	0.29(6)	0.05(1)
	3/2	0.80(8)	0.87(9)	0.82(12)	0.14(2)

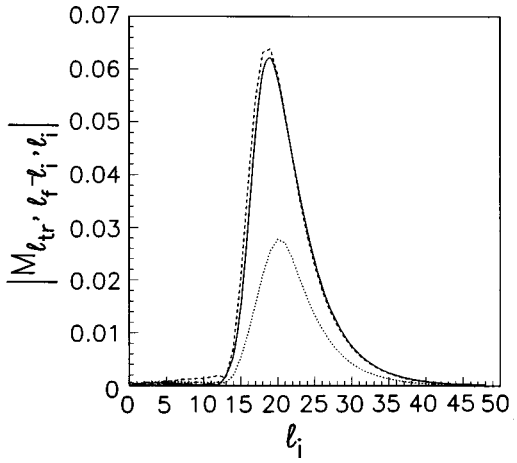

FIG. 12. The l_i dependence of the modulus of the partial wave reaction amplitudes $M_{l_{\rm tr},l_f-l_i,l_i}$ for the reaction ^{9}Be(^{10}B,^{9}Be)^{10}B at different $l_{\rm tr}$. Here l_i and l_f are the relative orbital angular momenta of the ^{10}B and ^{9}Be nuclei in the entrance and exit channels, respectively. The solid line is for $l_{\rm tr}=0$, $l_f-l_i=0$; the dashed line is for $l_{\rm tr}=1$, $l_f-l_i=0$; and the dotted line is for $l_{\rm tr}=2$, $l_f-l_i=-2$. In the latter case, the contributions with $l_f-l_i=0$ and $+2$ are comparable to the one shown.

DWBA with an optical potential which includes the deformation term. The difference between the coupled channels cross section and DWBA cross section is about 6%. This introduces an additional uncertainty of about 3% in the extracted C^2 for the ground state of ^{10}B.

Combining the uncertainties in R and our choice of optical model parameters with the statistical error in the DWBA fit and the additional normalization uncertainty in the data yields an overall uncertainty for the ground state C^2 of $\pm 9.0\%$. Thus for the ground state decay, we find $C^2=5.06\pm0.46$ fm^{-1}. The corresponding value of the ^{10}B ground state NVC is $|G|^2=0.87\pm0.08$ fm. This result agrees very well with the value of the ^{10}B ground state ANC derived from a recent analysis of the ^{9}Be(^{3}He,d)^{10}B reaction [34]. Since ^{9}Be(^{10}B,^{9}Be)^{10}B is the angular momentum matched reaction the multistep processes should not affect the cross section at small angles [33].

We have also analyzed the contribution of the different reaction partial wave amplitudes. In Fig. 12 we present the l_i dependence of the modulus of the reaction partial wave amplitudes for different $l_{\rm tr}$. The contribution to the reaction amplitude from lower partial waves $l_i<16$ is practically negligible due to the strong absorption in the entrance and exit channels. We note that the orbital angular momentum of the relative motion of the colliding nuclei is $k_iR_{\rm ch}\approx16$ for the channel radius $R_{\rm ch}\approx5$ fm. We found that $l_i>16$ are large enough that the uncertainties in the single-particle potentials have a very small influence on the calculated partial wave amplitudes. However, for these partial waves, rescattering effects in the initial and final states are still important. Only at $l_i>25$ does the contribution from rescattering become negligible, and the partial waves calculated for optical potentials 1 and 2 coincide. Thus the contribution of the partial waves between $16<l_i<25$ produces the difference in the ANC extracted using the two optical potentials.

For the transition ^{10}B(0.718 MeV)$\rightarrow^9$Be$+p$, the proton binding energy in the final state is 5.87 MeV, and the angular momenta are [30] $J_X^\pi=3^+$, $J_Y^\pi=J_A^\pi=3/2^-$, $J_B^\pi=1^+$, $l_X=l_B=1$, $j_X=3/2$, $j_B=1/2,3/2$. For the transition $j_X=3/2\rightarrow j_B=1/2$, the allowed $l_{\rm tr}=1,2$, and for $j_X=3/2\rightarrow j_B=3/2$, $l_{\rm tr}=0,1,2$. As for the previous case, the $l_{\rm tr}=0$ component is overwhelmingly dominant and provides the peak in the angular distribution at 0°. For this transition, as well as the subsequent ones that we discuss, we have verified that the reaction is peripheral with calculations similar to those described for the ground state transition. The experimental and calculated angular distributions are presented in Fig. 6. The ANC's extracted using potentials 1 and 2, as well as our adopted values for the ANC's and the corresponding NVC's, are given in Table III.

For the ^{10}B(1.740 MeV)$\rightarrow^9$Be$+p$ case, the proton binding energy in the final state is 4.847 MeV, and the angular momenta are [30] $J_X^\pi=3^+$, $J_Y^\pi=J_A^\pi=3/2^-$, $J_B^\pi=0^+$, $l_X=l_B=1$, $j_X=3/2$, $j_B=3/2$. The allowed $l_{\rm tr}=0,1,2$, and as above, the $l_{\rm tr}=0$ component is dominant. The experimental and calculated angular distributions for this reaction are presented in Fig. 7, and the ANC's are given in Table III.

For the ^{10}B(2.154 MeV)$\rightarrow^9$Be$+p$ transition, the proton binding energy in the final ^{10}B is 4.433 MeV, and the angular momenta are [30] $J_X^\pi=3^+$, $J_Y^\pi=J_A^\pi=3/2^-$, $J_B^\pi=1^+$, $l_X=l_B=1$, $j_X=3/2$, $j_B=1/2,3/2$. For the transition $j_X=3/2\rightarrow j_B=1/2$, the allowed $l_{\rm tr}=1,2$, and for $j_X=3/2\rightarrow j_B=3/2$, the allowed $l_{\rm tr}=0,1,2$. Once again, the $l_{\rm tr}=0$ component dominates. The experimental and calculated angular distributions are presented in Fig. 8, and the ANC's are given in Table III.

The analysis of ^{9}Be(^{3}He,d)^{10}B(0.718 MeV) [34] unfortunately cannot be used to extract unambiguously the individual values of C^2 for $j_{^{10}B*}=3/2$ and $j_{^{10}B*}=1/2$ since both transitions $j_{^{10}B}=3/2\rightarrow j_{^{10}B*}=3/2$ and $j_{^{10}B}=3/2\rightarrow j_{^{10}B*}=1/2$ give the same angular distributions in the (^{3}He,d) reaction. Thus, one advantage of using the heavy-ion reaction ^{9}Be(^{10}B,^{9}Be)^{10}B, compared to ^{9}Be(^{3}He,d)^{10}B, is that we are able to extract the C^2 for both transitions unambiguously by fitting the calculated angular distributions to the experimental one at forward angles ($\theta_{\rm c.m.}<20°$). The C^2 for the $T=1$ excited state at $E^*=1.740$ MeV can be determined by (^{3}He,d) since a single j and l in each vertex contributes to the reaction. In contrast to the very good agreement that was found for the ground state, the C^2 extracted from the heavy-ion-induced proton transfer reaction is a factor of 2 smaller than that obtained from (^{3}He,d). We note that this excited state is notorious for the difference found between spectroscopic factors extracted from the analysis of ^{9}Be(^{3}He,d)^{10}B and ^{9}Be(d,n)^{10}B [30]. It was shown that this difference can be significantly reduced within the framework of isospin-dependent DWBA [35]. Whereas the spectroscopic factor extracted from the analysis of the (d,n) reaction remains essentially unchanged in the two approaches, the isospin modified DWBA significantly decreases the spectroscopic factor extracted from the (^{3}He,d) reaction, bringing it closer to the spectroscopic factor extracted from the (d,n) reaction. Since isospins of the nuclei in the reactions ^{9}Be(^{10}B,^{9}Be)^{10}B(1.740 MeV) and ^{9}Be(d,n)^{10}B(1.740 MeV) are identical, we conclude that the value of the ANC extracted from the reaction ^{9}Be(^{10}B,^{9}Be)^{10}B(1.740 MeV) is more accurate than that ex-

tracted from the reaction ^{9}Be(^{3}He,d)^{10}B(1.740 MeV).

VI. SUMMARY

We have measured the differential cross sections for the reaction ^{9}Be(^{10}B,^{9}Be)^{10}B at 100 MeV, leading to the ground and first three excited states of ^{10}B. We also have measured the elastic scattering ^{9}Be(^{10}B,^{10}B)^{9}Be to determine the optical potential to be used in the analysis of the proton transfer reactions. Analysis shows that the measured proton transfer reactions are extremely peripheral. Therefore, we were able to extract the ANC's for proton removal from the ground and first three excited states of ^{10}B. Our primary goal was to extract the ANC for the virtual decay ^{10}B(g.s.)$\rightarrow^{9}$Be$+p$. Our final result agrees very well with the ANC found from the ^{9}Be(^{3}He,d)^{10}B reaction.

We are going to use the extracted ANC when analyzing the ^{10}B(^{7}Be,^{8}B)^{9}Be reaction to determine the ANC's for proton removal from ^{8}B: ^{8}B$\rightarrow^{7}$Be$+p$. These ANC's determine the normalization of the astrophysical cross section for the ^{7}Be$(p,\gamma)^{8}$B reaction. The measurements of the ^{10}B(^{7}Be,^{8}B)^{9}Be reaction are under way at the Texas A&M University Cyclotron Institute. In addition, the extracted ANC's for the virtual decays ^{10}B$\rightarrow^{9}$Be$+p$ of the ground and first three excited states of ^{10}B will be used to calculate the direct radiative capture contribution to the astrophysical reaction ^{9}Be$+p\rightarrow^{10}$B$+\gamma$.

We have also shown that heavy-ion-induced nucleon transfer reactions are a very useful tool to extract information about the normalization of the tail of nuclear bound state wave functions in the channel corresponding to proton removal. Such information can play a central role in calculating the reaction rates for the corresponding direct astrophysical radiative capture processes.

ACKNOWLEDGMENTS

This work was supported in part by the U.S. Department of Energy under Grant No. DE-FG05-93ER40773 and by the Robert A. Welch Foundation.

[1] A. M. Mukhamedzhanov and N. K. Timofeyuk, JETP Lett. **51**, 282 (1990).
[2] H. M. Xu, C. A. Gagliardi, R. E. Tribble, A. M. Mukhamedzhanov, and N. K. Timofeyuk, Phys. Rev. Lett. **73**, 2027 (1994).
[3] Z. R. Irwinski, L. Rosenberg, and L. Spruch, Phys. Rev. C **29**, 349 (1984).
[4] L. D. Blokhintsev, V. I. Kukulin, A. A. Sakharuk, D. A. Savin, and E. V. Kuznetsova, Phys. Rev. C **48**, 2390 (1993).
[5] A. M. Mukhamedzhanov, R. E. Tribble, and N. K. Timofeyuk, Phys. Rev. C **51**, 3472 (1995).
[6] C. A. Gagliardi, R. E. Tribble, J. Jiang, A. M. Mukhamedzhanov, L. Trache, H. M. Xu, S. J. Yennello, and X. G. Zhou, Nucl. Phys. **A588**, 327c (1995).
[7] A. M. Mukhamedzhanov and N. K. Timofeyuk, Sov. J. Nucl. Phys. **51**, 431 (1990).
[8] T. Motoboyashi *et al.*, Phys. Rev. Lett. **73**, 2680 (1994).
[9] F. G. Barker, Nucl. Phys. **A588**, 693 (1995).
[10] F. E. Cecil, D. Ferg, H. Liu, J. C. Scorby, J. A. McNeil, and P. D. Kunz, Nucl. Phys. **A539**, 75 (1992).
[11] D. Zahnow, C. Angulo, M. Junker, C. Rolfs, S. Schmidt, W. H. Schulte, and E. Somorjai, Nucl. Phys. **A589**, 95 (1995).
[12] H. P. Gubler, G. R. Plattner, L. Sick, and A. Traver, Nucl. Phys. **A284**, 114 (1977).
[13] S. Burzynski, M. Baumgartner, H. P. Gubler, J. Jourdan, H. O. Meyer, G. R. Plattner, H. W. Roser, and L. Sick, Nucl. Phys. **A399**, 230 (1977).
[14] L. Jarczyk, B. Kamys, A. Stralkowsky, A. Szczurek, M. Godlewski, J. Lang, R. Müller, and J. Sromiski, Phys. Rev. C **31**, 12 (1985).
[15] K. Bodek, M. Hugi, J. Lang, R. Müller, A. Schultz, J. Sromski, E. Ungricht, L. Jarczyk, and A. Stralkowski, Phys. Lett. **92B**, 79 (1980).
[16] R. M. DeVries, Phys. Rev. C **8**, 951 (1973).
[17] L. D. Blokhintsev, I. Borbely, and E. I. Dolinskii, Fiz. Elem. Chastits At. Yadra **8**, 1189 (1977) [Sov. J. Part. Nuclei **8**, 485 (1977)].
[18] L. D. Blokhintsev, A. M. Mukhamedzhanov, and A. N. Safronov, Fiz. Elem. Chastits At. Yadra **15**, 1296 (1984) [Sov. J. Part. Nuclei **15**, 580 (1984)].
[19] D. M. Pringle, W. N. Catford, J. S. Winfield, D. G. Lewis, N. A. Jelley, K. W. Allen, and J. H. Coupland, Nucl. Instrum. Methods Phys. Res. A **245**, 230 (1986).
[20] D. H. Youngblood and J. B. Bronson, Nucl. Instrum. Methods Phys. Res. A **361**, 37 (1995).
[21] D. H. Youngblood, Y.-W. Liu, H. L. Clark, P. Oliver, and G. Simler, Nucl. Instrum. Methods Phys. Res. A **361**, 539 (1995).
[22] S. Kowalski and H. A. Enge, computer code RAYTRACE (unpublished).
[23] J. F. Ziegler, computer code TRIM (unpublished).
[24] F. Carstoiu, computer code OPTIMINIX (unpublished).
[25] G. Igo, Phys. Rev. **115**, 1665 (1959).
[26] M. Rhoades-Brown, Steven Pieper, and M. McFarlane, computer code PTOLEMY, 1983 (unpublished).
[27] J. Raynal, Phys. Rev. C **23**, 2571 (1981).
[28] G. Bertsch, J. Borysowicz, H. McManus, and W. G. Love, Nucl. Phys. **A284**, 399 (1977).
[29] R. M. DeVries, Ph.D. thesis, University of California, 1971; J. L. Perrenoud and R. M. DeVries, Phys. Lett. **36B**, 18 (1971).
[30] F. Ajzenberg-Selove, Nucl. Phys. **A490**, 1 (1988).
[31] D. M. Brink, Phys. Lett. **40B**, 37 (1972).
[32] P. D. Kunz, computer code CHUCK, University of Colorado (unpublished).
[33] M. N. Harakeh, J. van Popta, A. Saha, and R. H. Siemssen, Nucl. Phys. **A344**, 15 (1980).
[34] V. Burjan, J. Cejpek, V. Kroha, A. Mukhamedzhanov, S. Piskor, R. E. Tribble, and J. Vincour, in *Proceedings of the Conference of Czech and Slovak Physicists*, Ostrava, Czech Republic, 1996 (unpublished).
[35] K. W. Kemper, S. Cotanch, G. E. Moore, A. W. Obst, R. J. Puigh, and R. L. White, Nucl. Phys. **A222**, 173 (1974).